High-Resolution Reconstruction of Sparse Data from Dense Low-Resolution Spatio-Temporal Data

Qing Yang and Bahram Parvin, *Senior Member, IEEE*

***Abstract*— A novel approach for reconstruction of sparse high-resolution data from lower-resolution dense spatio-temporal data is introduced. The basic idea is to compute the dense feature velocities from lower-resolution data and project them to the corresponding high-resolution data for computing the missing data. In this context, the basic flow equation is solved for intensity, as opposed to feature velocities at high resolution. Although the proposed technique is generic, we have applied our approach to sea surface temperature (SST) data at 18 km (low-resolution dense data) for computing the feature velocities and at 4 km (high-resolution sparse data) for interpolating the missing data. At low resolution, computation of the flow field is regularized and uses the incompressibility constraints for tracking fluid motion. At high resolution, computation of the intensity is regularized for continuity across multiple frames.**

***Index Terms*— High resolution, interpolation, motion, duality, multigrid methods**

I. Introduction

This paper presents a novel approach for reconstruction of high-resolution spatio-temporal data from lower-resolution data. The development of the proposed system is driven by the need to fill in missing data in high-resolution images obtained from observational platforms. Current environmental satellites generate massive amount of *sparse* geophysical data, e.g., sea surface temperature (SST), ocean color, and precipitation data. These observations are collected through the NASA MODIS (50-100 gigabytes/day of oceanic data) and NOAA AVHRR (4 gigabytes/day) spacecraft. Global AVHRR data are down-linked to several universities and managed by an automatic processing environment that navigates, calibrates, and computes the geophysical fields (e.g., SST) and combines the satellite swath data into daily, regional, and global fields. In the case of SST, the sparseness of data is due to cloud and aerosol contamination. These data need to be interpolated for effective visualization and subsequent analysis. We focus on dense reconstruction of sparse SST data at 4 km resolution. An example of sparse SST data at high resolution is shown in Figure 1. The novelty of our work is not just limited to the proposed methods, but also to the fact that current reconstruction (interpolation) algorithms do not scale to 4 km data due to computational complexities. Our approach consists of three steps:

1) Leveraging the current operational low-resolution reconstruction techniques at 18 km.
2) Computing feature velocities of dense spatio-temporal images from low-resolution 18 km data.
3) Projecting computed feature velocities onto 4 km data and solving the flow equation for intensity as opposed to velocities.

Manuscript received 5 Jun. 2001; accepted 22 Jan. 2003.
Recommended for acceptance by Dr. Arnaud Jacquin.
The authors are with the Imaging and Informatics Group of the Computational Research Division at Lawrence Berkeley National Laboratory, Berkeley, CA 94720

Current methods for interpolating SST data are based on objective analysis (OA) [1] and optimal interpolation (OI) [2] as a special case. These techniques operate on randomly distributed spatio-temporal data, and they have been shown to be reliable up to 18 km resolution, e.g., a grid size of $0.25°$ with an image size of 720×1440. However, due to the extremely high computational complexity of these methods, interpolating SST data at high resolution, e.g., a grid size of $(0.04395°$ with an image size of 4096×8192, remains an open problem. We propose to solve this problem by integrating two different sources of information: *motion* and *temperature*. In the proposed model, we can incorporate flow, temperature, incompressibility and smoothness together. As we shall see, the temperature gradient and oceanic flow are dual, and if one is known, the other can be computed. In this context, given an estimate of oceanic flow, we can interpolate the SST data by a "fix one and compute the other" strategy.

We show that our model can also be applied to a sequence of high-resolution SST data where each frame has a corresponding lower-resolution optical flow representation. This is similar to the MPEG-1 standard, where motion is computed at a low resolution to predict the next frame. The error in the prediction is then corrected by the regularization term. There is a close similarity between this model and the related Bayesian framework [3]–[5].

The outline of this paper is as follows. An overview of previous work and background material is presented in Section II. Section III describes the basic idea and its detailed implementation. Section IV gives the experimental results. Section V concludes the paper.

II. Previous work

In this section, a brief summary of objective analysis, Bayesian models, and the Gibbs sampler is provided. Introduction to traditional super-resolution restoration can be found in [6]–[8].

A. Objective analysis

Objective analysis (OA) is used extensively by meteorologists [9] and oceanographers [1] for estimating the values of geophysical variables at a grid of interpolation points from

Fig. 1. Sample sea surface temperature (SST) data with no interpolation.

irregularly distributed data points. OA is based on the Gauss-Markoff theorem for a linear minimum mean-square estimate of a random variable and requires the estimates of the first and second order statistics for both the observing and the dynamical system.

The most common method of objective analysis in current operational numerical forecast centers is the optimal interpolation (OI) method. This method uses predefined covariance functions derived from climatological data in order to relate the covariance between the field at a grid point and the observation point. The OI analysis is discussed in [2] where the analysis is computed in terms of increments, rather than the actual temperatures, so that the initial guess is preserved in regions with little or no data. Presently, the OI analysis is produced for daily and weekly periods on a 1° grid. Since local conditions tend to persist for a time, the previous OI analysis is used as a first guess for the next analysis. This was found to be more accurate than using climatology as an initial guess. To reduce the number of observations used in the OI, averages over 1° squares are computed. These "super observations" are computed independently per ship and buoy identification code and for the day and night of satellite retrievals. Ships normally make only one 6-hourly report, in a given grid box. As a result, the chief effect of this averaging is to reduce the number of buoy and satellite measurement values used in the analysis. The analysis increment is defined as the difference between the analysis and the first guess; the data increment is defined as the difference between the data and the first guess. The analysis increment, $r(k)$, is given by $r(k) = \sum_i w(i,k)q(i)$ where $q(i)$ are the data increments and $w(i,k)$ are the least square weights. The subscript (k) ranges over the grid points where the solution is required and the subscript (i) ranges over the data points. When there is little or no data in a region, the weights $w(i,k)$ approach zero. The OI method is only optimal when the correlations and variances needed to calculate the $w(i,k)$ are known for incremental analysis. Calculation of the $w(i,k)$ involves matrix inversions that become unstable if too many data points are involved. This is one reason that averages over the grid squares are formed before the analysis. The ship measurements are noisier than the buoy and satellite measurements, and they have smaller weight values in the analysis.

OI is a widely accepted method in the community, and it has been used by NOAA-CIRES Climate Diagnostics Center to generate weekly sea surface temperature data with one-degree resolution. However, all existing OA-based techniques fail to interpolate SST data on higher-resolution grids, e.g., 4096×8192, due to instability and increased computational complexity.

B. Bayesian framework

Statistical inference has been used for analyzing and understanding images for at least 20 years [3], [10], [11]. A brief introduction to this topic can be found in [5]. In general, such a model consists of two parts: a *prior model* of possible parameters, and a *data model* of what images are consistent with this prior model of the scene. Let w be the variables to describe the scene; the model is completed by giving the conditional probabilities $\pi(I|w)$ of any image I given the scene variables w, resulting in the joint probability distribution:

$$\pi(I, w) = \pi(I|w) \cdot \pi(w) \tag{1}$$

Using Bayes' theorem, we have

$$\pi(w|I) = \frac{\pi(I|w) \cdot \pi(w)}{\pi(I)} \propto \pi(I|w) \cdot \pi(w) \tag{2}$$

The corresponding energy is expressed as

$$\begin{aligned} E(w) &= -\log(\pi(w|I)) = -\log(\pi(I|w)) - \log(\pi(w)) \\ &= E_d(I, w) + E_p(w) \end{aligned} \tag{3}$$

where the goal is now to minimize $E(w)$. E_p is sometimes called the regularizer because it was historically introduced to make the variational problem of minimizing E_d well-posed.

Although the above framework is rather simple, it has proven to be powerful. It is not sufficient to propose various energy models – an efficient solution is also needed. Among all computer simulation methods, the Monte Carlo methodology, especially Markov Chain Monte Carlo (MCMC), provides an enormous scope for statistical modeling, which has attracted much attention among statisticians. MCMC is a well accepted technique for integrating over high-dimensional probability distributions, including situations with missing data and nuisance parameters, and may be used to make inference for parameters of interest.

In the next section, we will introduce two special samplers in MCMC, i.e., Gibbs sampler [4] and two-component Gibbs sampler.

C. Gibbs sampler

Let

$$\pi(x) = \frac{1}{Z} \exp(-E(x)) \tag{4}$$

be the target probability distribution function under investigation, where $E(x)$ is the energy, and Z is the normalizing constant. Suppose $x = (x_1, x_2, \cdots, x_d)$, and the current state is $x^{(t)} = (x_1^{(t)}, x_2^{(t)}, \cdots, x_d^{(t)})$, where d is the dimension. Then the systematic scan Gibbs sampler can be described as follows:

- For $i = 1, \cdots, d$, we draw $x_i^{(t+1)}$ from the conditional distribution

$$\pi(x_i | x_1^{(t+1)}, \cdots, x_{i-1}^{(t+1)}, x_{i+1}^{(t)}, \cdots, x_d^{(t)}) \tag{5}$$

In summary, to update one variable, we fix all other variables, and draw a sample from the conditional probability. Gibbs sampler was proposed by Geman and Geman [4], which effectively reduces a high-dimensional simulation problem to a series of lower-dimensional ones, Thus, reducing the complexities of large-scale problems. In practical applications, highly correlated variables are often grouped together for blocking Gibbs sampling. Among various grouping schemes, the two-component Gibbs sampler is of particular interest, which operates as follows. If a random variable x can be partitioned into two parts, $x = (x_1, x_2)$ with the current state at $(x_1^{(t)}, x_2^{(t)})$, then a two-component Gibbs sampler [4] updates as:

- Draw $x_1^{(t+1)}$ from conditional distribution $\pi_{1|2}(\cdot|x_2^{(t)})$;
- Draw $x_2^{(t+1)}$ from conditional distribution $\pi_{2|1}(\cdot|x_1^{(t)})$.

This sampler corresponds to the data augmentation algorithm [12], which was designed for handling Bayesian missing data problems. This idea is closely related to the EM algorithm [13], which is widely used by computer vision researchers [14].

III. Duality of feature velocity measurement and reconstruction

Let $I^{(t)}(x, y)$ be a sequence of SST data where x and y correspond to latitude and longitude, t is the time, and I is the actual temperature. Let $(u^{(t)}(x, y), v^{(t)}(x, t))$ represent the corresponding feature displacement velocity (FDV) at each point, where u and v are the horizontal and vertical velocity respectively. The energy governing computation of FDV equation for incompressible fluid can be expressed as (subscripts represent partial derivatives in this paper)

$$\iint (I_x u + I_y v + I_t)^2 + \alpha^2(u_x^2 + u_y^2 + v_x^2 + v_y^2) + \beta^2(u_x + v_y)^2 + \gamma^2(I_x^2 + I_y^2)dxdy \quad (6)$$

This equation assumes brightness constancy, i.e.,

$$I_x u + I_y v + I_t \approx 0 \quad (7)$$

which is exactly the same constraint as the Horn-Schunck optical flow model [15]. The first term in Equation 6 is the simplified two-dimensional conservation of temperature. The second term is the spatial smoothness constraint on the FDV. The third term is the zero-divergence constraint when β is set to a large number. For incompressible fluids, the fluid motion has to have zero divergence at each point, i.e., $u_x + v_y = -w_z$, where w is the component in the z direction. Under weak constraints, this equation can be expressed as $u_x + v_y \approx 0$. A vector field with zero-divergence does not contain sinks and sources. A counter example is given in Figure 2. The fourth term is the smoothness of the temperature. This new constraint is necessary for the interpolation (reconstruction) problem.

In general, all the unknowns in Equation 6 can be solved simultaneously, but this is a difficult nonlinear problem that cannot be solved in a reasonable time span. However, the duality of Equation 6

$$(I_x, I_y, I_t) \cdot (u, v, 1)^T = 0 \quad (8)$$

indicates that if the FDV is fixed, then the intensity can be computed with additional constraints and vice-versa.

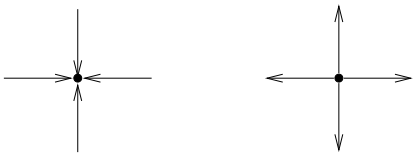

Fig. 2. Critical points with non-zero divergence: (left) a sink; (right) a source.

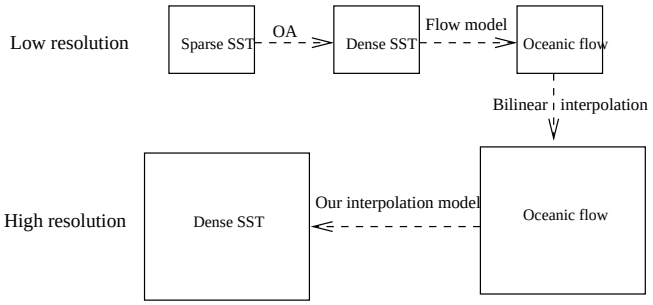

Fig. 3. Protocol for reconstructing (interpolating) high-resolution SST data.

If the temperature is known at each point, then the following model is used to estimate the FDV

$$\frac{1}{2}\iint (I_x u + I_y v + I_t)^2 + \alpha^2(u_x^2 + u_y^2 + v_x^2 + v_y^2) + \beta^2(u_x + v_y)^2 dxdy \quad (9)$$

This model has been studied in [16], [17], and can be solved efficiently. On the other hand, if (u, v) is known, then Equation 6 reduces to

$$\frac{1}{2}\iint (I_x u + I_y v + I_t)^2 + \gamma^2(I_x^2 + I_y^2)dxdy \quad (10)$$

Although the above strategy is feasible, the computational cost is too high in the absence of a good initial condition. This initial condition is derived from the low-resolution dense SST data through OA analysis. Extending SST from low-resolution to high resolution provides a good initial solution. However, the computational cost of FDV at a high resolution, e.g., 4 km, is still too high. As a result, we compute the flow at the low resolution, then project the *FDV* to the high resolution. This is a multi-resolution version of the two-component sampler described in the previous section.

Figure 3 shows our approach to high-resolution reconstruction of sparse SST data which takes advantage of the dual representation of Equation 6. We solve the FDV at low resolution and then project it to high resolution for reconstruction using the known velocity field. The concept of "*fix one part and compute the other*" is utilized in the absence of random sampling.

A. Computing velocity field at low resolution

Equation (9) is essentially the generalization of of Horn and Schunck's optical flow model [15]. A weak zero-divergence constraint is added to form this new energy functional. This model has been studied by Suter [16], Gupta and Prince [17] and Yang and Parvin [18]. Our implementation uses a multigrid method for high efficiency. We have tested our technique on several years of SST data and compared the computed velocity with ground truth data obtained from buoy

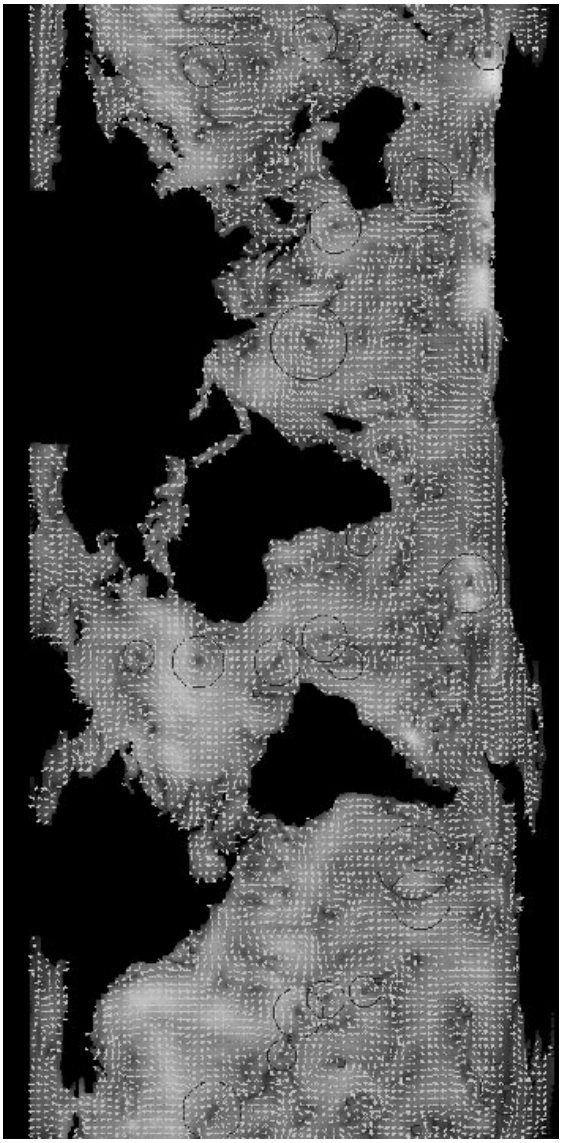

Fig. 4. Computed feature velocities, their magnitude (as underlying intensity), and vortices from a pair of images at low resolution (18 km).

measurement. Figure 4 shows an example of the computation of velocity field at 18 km resolution.

The corresponding Euler-Lagrange equations for Equation (9) are given by

$$\begin{cases} -I_x(I_x u + I_y v + I_t) + (\alpha^2+\beta^2)u_{xx} + \alpha^2 u_{yy} + \beta^2 v_{xy} = 0 \\ -I_y(I_x u + I_y v + I_t) + \alpha^2 v_{xx} + (\alpha^2+\beta^2)v_{yy} + \beta^2 u_{xy} = 0 \end{cases} \tag{11}$$

Substituting the finite difference representation of u's (and similarly v's) partial derivatives

$$\begin{aligned} u_{xx}|_{j,i} &= \tfrac{u_{j+h,i}+u_{j-h,i}-2u_{j,i}}{h^2} \\ u_{yy}|_{j,i} &= \tfrac{u_{j,i+h}+u_{j,i-h}-2u_{j,i}}{h^2} \\ u_{xy}|_{j,i} &= \tfrac{u_{j+h,i+h}+u_{j-h,i-h}-u_{j+h,i-h}-u_{j-h,i+h}}{4h^2} \end{aligned} \tag{12}$$

into Eq. (11), we have

$$\begin{cases} (I_x^2 + \frac{4\alpha^2+2\beta^2}{h^2})u_{j,i} + I_x I_y v_{j,i} = \Delta_1 \\ I_x I_y u_{j,i} + (I_y^2 + \frac{4\alpha^2+2\beta^2}{h^2})v_{j,i} = \Delta_2 \end{cases} \tag{13}$$

where

$$\Delta_1 = -I_x I_t + \tfrac{\alpha^2+\beta}{h^2}(u_{j+h,i} + u_{j-h,i}) + \tfrac{\alpha^2}{h^2}(u_{j,i+h} + u_{j,i-h}) + \tfrac{\beta^2}{4h^2}(v_{j+h,i+h} + v_{j-h,i-h} - v_{j+h,i-h} - v_{j-h,i+h})$$

$$\Delta_2 = -I_y I_t + \tfrac{\alpha^2}{h^2}(v_{j+h,i} + v_{j-h,i}) + \tfrac{\alpha^2+\beta}{h^2}(v_{j,i+h} + v_{j,i-h}) + \tfrac{\beta^2}{4h^2}(u_{j+h,i+h} + u_{j-h,i-h} - u_{j+h,i-h} - u_{j-h,i+h})$$

Representing $u_{j,i}$ and $v_{j,i}$ by Δ_1 and Δ_2, we have the following iterative strategy

$$\begin{cases} u_{j,i}^{(n+1)} = \frac{1}{D}[(I_y^2 + \frac{4\alpha^2+2\beta}{h^2})\Delta_1^{(n)} - I_x I_y \Delta_2^{(n)}] \\ v_{j,i}^{(n+1)} = \frac{1}{D}[-I_x I_y \Delta_1^{(n)} + (I_x^2 + \frac{4\alpha^2+2\beta}{h^2})\Delta_2^{(n)}] \end{cases} \tag{14}$$

where $(u_{j,i}^{(n)}, v_{j,i}^{(n)})$ is the velocity field at the n-th step, $D = \frac{4\alpha^2+2\beta^2}{h^2}(I_x^2 + I_y^2) + (\frac{4\alpha^2+2\beta^2}{h^2})^2$.

B. Computing intensity at high resolution

By projecting computed feature velocities at low resolution to sparse high-resolution data, we now can fill in the missing intensity data (temperature). Let $I^{(t-1)}(x,y)$ and $I^{(t)}(x,y)$ be a consecutive pair of SST images, the brightness constancy constraint is given by

$$I_x^{(t-1)}u^{(t-1)} + I_y^{(t-1)}v^{(t-1)} + I^{(t)} - I^{(t-1)} = 0 \tag{15}$$

or

$$I^{(t)} = -I_x^{(t-1)}u^{(t-1)} - I_y^{(t-1)}v^{(t-1)} + I^{(t-1)} \tag{16}$$

If $I^{(t-1)}$ is fixed, then an estimate of $I^{(t)}$ is

$$\widehat{I}^{(t)} = -I_x^{(t-1)}u^{(t-1)} - I_y^{(t-1)}v^{(t-1)} + I^{(t-1)} \tag{17}$$

Equation (10) can be rewritten as

$$\frac{1}{2}\iint (I - \widehat{I})^2 + \gamma^2(I_x^2 + I_y^2)dxdy \tag{18}$$

and the corresponding Euler-Lagrange equation is now given by

$$I = \widehat{I} + \gamma^2 \triangle I \tag{19}$$

which is a very simple elliptic PDE. Substituting the finite difference operator of $\triangle I$

$$\triangle I_{j,i} = \tfrac{I_{j+h,i}+I_{j-h,i}+I_{j,i+h}+I_{j,i-h}-4I_{j,i}}{h^2} \tag{20}$$

into Equation (19) yields

$$I_{j,i} = \widehat{I}_{j,i} + \gamma^2 \tfrac{I_{j+h,i}+I_{j-h,i}+I_{j,i+h}+I_{j,i-h}-4I_{j,i}}{h^2} \tag{21}$$

and the iterative equation is now given by

$$I_{j,i} \leftarrow \tfrac{h^2\widehat{I}_{j,i}+\gamma^2(I_{j+h,i}+I_{j-h,i}+I_{j,i+h}+I_{j,i-h})}{h^2+4\gamma^2} \tag{22}$$

The detailed multigrid implementation of this algorithm is as follows.

- STEP 0. $h = 2^K$
- STEP 1. Repeat the following algorithm until it converges for $(i = 0; i < M; i = i + h)$ for $(j = 0; j < N; j = j + h)$ let

$$I_{j,i} \leftarrow \frac{h^2\widehat{I}_{j,i} + \gamma^2(I_{j+h,i} + I_{j-h,i} + I_{j,i+h} + I_{j,i-h})}{h^2 + 4\gamma^2} \tag{23}$$

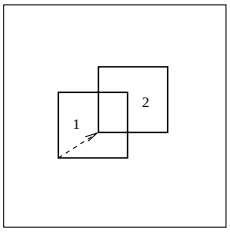

Fig. 5. MPEG-1 compression standard.

where $M \times N$ is the image size, $(I_{j,i}$ is the temperature at location (j, i).

- STEP 2. Linear interpolation.
  for $(i = 0; i < M; i++)\{$
  $i_0 = [i/h] \cdot h, r_i = (i - i_0)/h;$
  for $(j = 0; j < N; j++)$ $\{$

$$\begin{aligned} &j_0 = [j/h] \cdot h, r_j = (j - j_0)/h; \\ &I_{j,i} = (1 - r_i)(1 - r_j) I_{j_0,i_0} + r_i(1 - r_j) I_{j_0,i_0+h} + \\ &(1 - r_i) r_j I_{j_0+h,i_0} + r_i r_j I_{j_0+h,i_0+h} \end{aligned} \tag{24}$$

  $\}$
  $\}$
- STEP 3. if $h = 1$, stop; else $h = h/2$, goto STEP 1.

The regularization process helps to confirm the estimate by checking the compatibility with existing points, and to reduce the error propagated between a pair of images.

C. Relation to MPEG-1 standard

Let us review the MPEG-1 standard. The basic scheme for compressing a video sequence is to predict the motion from frame to frame in time, and then to use DCTs (discrete cosine transforms) to organize the redundancy in the spatial directions. The DCTs are computed on 8x8 blocks, and the motion prediction is done on 16x16 blocks. In other words, given a 16x16 block in the current frame that needs to be compressed, we look for a close match to that block in a previous or future frame. Figure 5 demonstrates this concept. If we know the accurate value on block 1 and its motion to the next frame, we can simply *copy* and *move* this block to its *new* location, e.g., block 2 of the next frame, if the data are missing there. In the case of the SST interpolation problem, the size of each block is $(4096/720) \times (8192/1440)$, or approximately 6×6. If the motion of a block of this size is known, then it can help us to predict the next frame with high accuracy. This is another way to present why we have avoided computing oceanic flow at high resolution.

D. Multi-frame interpolation

Interpolation can be extended to multiple frames by rewriting Equation (10) as

$$\begin{aligned} &E(I^{(1)}, \ldots, I^{(T)}) = \tfrac{1}{2} \textstyle\sum_{t=1}^{T} \iint [I_x^{(t)} u + I_y^{(t)} v + I_t^{(t)}]^2 + \\ &\gamma^2 [{I_x^{(t)}}^2 + {I_y^{(t)}}^2] dx dy \end{aligned} \tag{25}$$

This conditional probability can be approximated by

$$\begin{aligned} &\pi(I^{(t)} | I^{(1)}, \ldots, I^{(t-1)}, I^{(t+1)}, \ldots, I^{(T)}) \propto \\ &\exp(-E(I^{(t)} | I^{(1)}, \ldots, I^{(t-1)}, I^{(t+1)}, \ldots, I^{(T)})) \end{aligned} \tag{26}$$

where

$$\begin{aligned} &E(I^{(t)} | I^{(1)}, \ldots, I^{(t-1)}, I^{(t+1)}, \ldots, I^{(T)}) = \\ &\tfrac{1}{2} \iint [I_x^{(t-1)} u^{(t-1)} + I_y^{(t-1)} v^{(t-1)} + I^{(t)} - I^{(t-1)}]^2 \\ &+ [I_x^{(t+1)} u^{(t+1)} + I_y^{(t+1)} v^{(t+1)} + I^{(t+1)} - I^{(t)}]^2 \\ &+ \gamma^2 [{I_x^{(t)}}^2 + {I_y^{(t)}}^2] dx dy \end{aligned} \tag{27}$$

Let

$$\begin{aligned} \widehat{I}^{(t|t-1)} &= -I_x^{(t-1)} u^{(t-1)} - I_y^{(t-1)} v^{(t-1)} + I^{(t-1)} \\ \widehat{I}^{(t|t+1)} &= I_x^{(t+1)} u^{(t+1)} + I_y^{(t+1)} v^{(t+1)} + I^{(t+1)} \end{aligned} \tag{28}$$

Then Equation (27) can be rewritten as

$$\begin{aligned} &E(I^{(t)} | I^{(1)}, \ldots, I^{(t-1)}, I^{(t+1)}, \ldots, I^{(T)}) = \\ &\tfrac{1}{2} \iint [I^{(t)} - \widehat{I}^{(t|t-1)}]^2 + [I^{(t)} - \widehat{I}^{(t|t+1)}]^2 + \\ &\gamma^2 [{I_x^{(t)}}^2 + {I_y^{(t)}}^2] dx dy \end{aligned} \tag{29}$$

with the corresponding Euler-Lagrange equation

$$I^{(t)} = \frac{\widehat{I}^{(t|t-1)} + \widehat{I}^{(t|t+1)}}{2} + \frac{\gamma^2}{2} \triangle I^{(t)} \tag{30}$$

which can be summarized as follows:

1) Predict the current frame from the previous frame.
2) Predict the current frame from the next frame.
3) Average the two predictions.
4) Smooth the average.

To a certain degree, this is adopted from the *systematic scan* (blocking) of Gibbs sampler [4] introduced in Section II-C. By applying the multi-frame optimization repeatedly, continuity of interpolating images is significantly improved.

IV. Experimental Results

We have validated our approach by removing dense regions in sparse high-resolution data followed by its reconstruction and comparison to the original data. Figure 6 shows the images used for validation. Computed error is very small.

Figures 7 and 8 show experimental results of our approach. Figures 7a and 7b correspond to the original sparse SST data and its quality field, respectively. The white pixels in Figure 7b indicate that the corresponding points in Figure 7a are highly unreliable. Figure 8a shows the dense SST data at low resolution where the flow field is computed. This dense data is reconstructed by objective analysis. The image has been enlarged to match the size of corresponding high-resolution data. This region corresponds to a $20° \times 20°$ region centered on 140° west and 30° north. Figure 8b is the interpolation result of Figure 7a, which shows a high-resolution dense image of the temperature distribution. A video of reconstruction results over a 30-day period is available at: *http://vision.lbl.gov/People/qyang/sst*

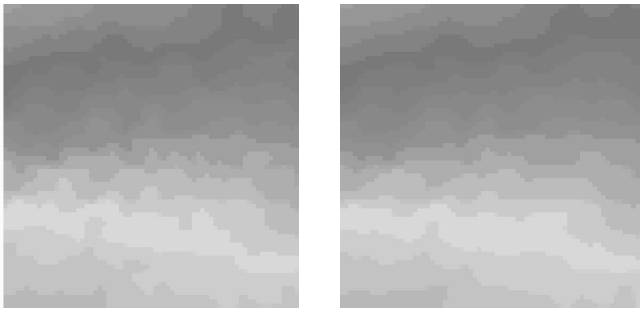

(a) (b)

Fig. 6. Reconstruction results: (a) original region that was removed from low-resolution SST data; (b) reconstruction of missing region.

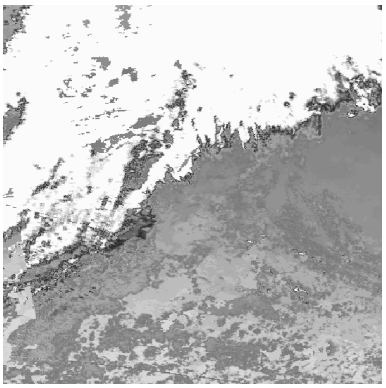

(a)

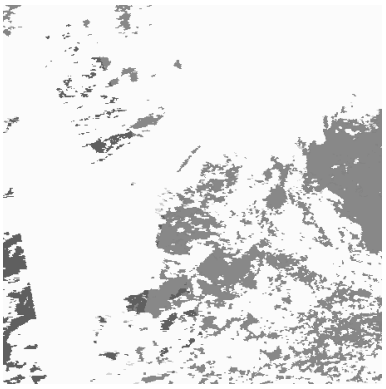

(b)

Fig. 7. SST data and quality field: (a) original SST data to be interpolated (date: the 40th day of 1998, longitude: 150W-130W, latitude: 20N-40N); (b) quality field: white pixels indicate that the corresponding points on (a) are highly unreliable or missing.

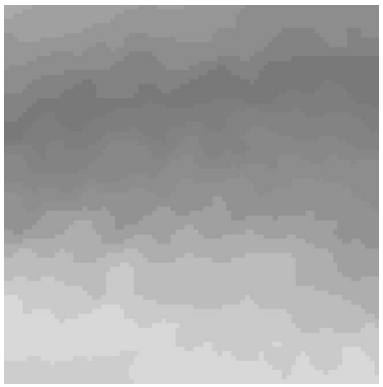

(a)

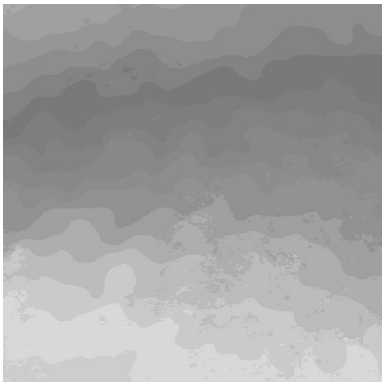

(b)

Fig. 8. Reconstruction of sparse SST data for Figure 7a: (a) dense SST data at low resolution (720×1440); (b) interpolated SST data at high resolution (4096×8192).

V. Conclusion

Interpolation of large-scale geophysical data is an open problem. This paper has proposed a new solution, applied it to real data, and validated the results. The basic idea is to leverage current operational interpolation techniques that are effective at low resolution to compute the corresponding feature velocities. Missing data at high resolution are then estimated by projecting computed feature velocities and solving the basic flow equation in reverse.

Acknowledgment

Research was funded by the Director of Lawrence Berkeley National Laboratory, and by the Mathematical and Information and Computing Sciences Division of the U.S. Department of Energy under Contract No. DE-AC03-76F00098 with the University of California. The publication number is LBNL-52152.

References

[1] F. P. Bretherton, R. E. Davis, and C. B. Fandry, "A technique for objective analysis and design of oceanographic experiments applied to mode-73," *Deep-Sea Res.*, vol. 23, pp. 559–582, 1976.

[2] R. W. Reynolds and T. M. Smith, "Improved global sea surface temperature analyses," *J. Climate*, vol. 7, pp. 929–948, 1994.
[3] U. Grenander, *Lectures in pattern theory 1, 2, and 3*. Springer, 1976-1981.
[4] S. Geman and D. Geman, "Stochastic relaxation, Gibbs distribution and Bayesian restoration of images," *IEEE Transactions on Pattern Analysis and Machine Intelligence*, vol. 6, pp. 721–741, 1984.
[5] D. Mumford, "The Bayesian rationale for energy functionals," *Geometry-Driven Diffusion in Computer Vision, Bart Romeny, Ed. by Kluwer Academic*, pp. 141–153, 1994.
[6] R. Schultz and R. Stevenson, "Extraction of high-resolution frames from video sequences," *IEEE Transactions on Image Processing*, vol. Vol 5, 1996.
[7] M. Elad and A. Feuer, "Restoration of single super-resolution image from several blurred noisy and down-sampled measured images," *IEEE Transactions on Image Processing*, vol. Vol 6, 1997.
[8] S. Baker and T. Kanade, "Limits on super-resolution and how to break them," *IEEE Transactions on Pattern Analysis and Machine Intelligence*, vol. V24, 2002.
[9] J.J. Thiebaux and M.A. Pedder, "Spatial objective analysis with applications in atmosphere science," *Acedemic Press, New York*, 1987.
[10] D. Cooper, "Maximum likelihood estimation of Markov process blob boundaries in noisy images," *PAMI*, vol. 1, pp. 372–384, 1979.
[11] D. Mumford and B. Gidas, "Stochastic models for generic images," *technical report*, 2000.
[12] M. Tanner and W. Wang, "The calculation of posterior distribution by data augmentation(with discussion)," *J. Amer. Statist. Assoc.*, vol. 82, pp. 528–550, 1987.
[13] A. Dempster, N. Laird, and D. Rubbin, "Maximum likelihood estimation from incomplete data via the EM algorithm(with discussion)," *J. Roy. Statist. Soc.*, vol. B 39, pp. 1–38, 1977.
[14] Y. Weiss and E. Adelson, "A unified mixture framework for motion segmentation: incorporating spatial coherence and estimating the number of models," in *CVPR'96*, San Francisco, California, 1996, pp. 321–326.
[15] B. K. P. Horn and B. G. Schunck, "Determining optical flow," *Artificial Intelligence*, vol. 17, pp. 185–203, 1981.
[16] D. Suter, "Motion estimation and vector splines," in *CVPR'94*, Seatle, WA, 1994, pp. 939–948.
[17] S. Gupta and J. Prince, "Stochastic models for div-curl optical flow methods," *IEEE Signal Processing Letters*, vol. 3(2), pp. 32–34, 1996.
[18] Q. Yang and B. Parvin, "Feature-based visualization of large scale geophysical data," in *CVPR'00*, vol. 2, Hilton Head Island, South Carolina, 2000, pp. 276–281.

Qing Yang is a computer scientist in the Computational Research Division at Lawrence Berkeley National Laboratory. His research interests include image processing, pattern recognition and bioinformatics. He received a Ph.D. in computer science from the Institute of Automation, Chinese Academy of Sciences. Contact him at: qyang@media.lbl.gov.

Bahram Parvin is a staff scientist in the Computational Research Division of Lawrence Berkeley National Laboratory. He conducts research on bioimaging, feature-based representation of time varying scientific images, and distributed informatics systems. He received his Ph.D. in Electrical Engineering from the University of Southern California in 1991. He is a senior member of IEEE.